The Hα Emission Line Variations of HR 6819

Douglas R. Gies [ORCID] and Luqian Wang (王璐茜) [ORCID]

Center for High Angular Resolution Astronomy and Department of Physics and Astronomy, Georgia State University, P.O. Box 5060, Atlanta, GA 30302-5060, USA; gies@chara.gsu.edu, lwang@chara.gsu.edu

Received 2020 June 23; revised 2020 July 10; accepted 2020 July 11; published 2020 July 30

Abstract

The star system HR 6819 was recently proposed by Rivinius et al. as the site of the nearest example of a stellar-mass black hole. Their spectra show evidence of two components: a B3 III star in a 40 day orbit and a stationary B-emission line star. Based upon the orbital mass function and the lack of evidence of a spectral component with reflex orbital motion, Rivinius et al. suggested that HR 6819 is a triple system consisting of an inner B3 III star plus black hole binary orbited by a distant Be star. Here we present an alternative model based upon an examination of the Hα emission line in their spectra. We show that the emission line displays the small reflex motion expected for the companion in the inner orbit and shows variations in profile shape related to orbital phase. This indicates that HR 6819 is a binary system consisting of a massive Be star and a low-mass companion that is the stripped down remnant of a former mass donor star in a mass transfer binary.

Unified Astronomy Thesaurus concepts: Binary stars (154); White dwarf stars (1799); Circumstellar disks (235)

1. Introduction

Rivinius et al. (2020) recently presented a spectroscopic investigation of the bright, early-type multiple system HR 6819 (HD 167128, QV Tel). Their analysis shows that the spectrum is dominated by three spectral components: a narrow-lined B3 III star in a 40 day orbit, a stationary Be star, and continuum and emission line flux from the disk surrounding the Be star. The orbital mass function and probable mass of the B3 III star indicate that the companion is massive ($>4.2\,M_\odot$), yet its expected spectral features are absent from the spectrum. This led Rivinius et al. (2020) to suggest that the companion is a non-accreting and X-ray-quiet black hole and that the Be star is a distant tertiary component.

There is growing evidence that many Be stars are the product of mass transfer in an interacting binary (Pols et al. 1991). The initially more massive component in a close binary is the first to expand after core hydrogen exhaustion, and as it reaches the dimensions of the critical Roche surface, it will begin to transfer mass and angular momentum to the companion star. If the system avoids a merger, the donor star will end up as a low-mass core stripped of its envelope, and the mass gainer will appear as a rejuvenated, fast-rotating, main-sequence star. Be stars are fast-rotating objects that are shedding angular momentum into an outflowing decretion disk (Rivinius et al. 2013), so they are potential candidates of systems spun up by binary mass transfer. The stripped companions are generally faint and difficult to detect, but spectroscopic searches in the ultraviolet part of the spectrum have begun to reveal the spectral lines of the hot, low-mass companions (Wang et al. 2018).

The presence of a Be star component in the spectrum of HR 6819 suggests another interpretation of the system. It is possible that the B3 III stellar component is actually a low-mass, stripped down star that is still relatively young and luminous. In this case, the Be star would be the companion in the 40 day binary instead of a black hole, and it should exhibit the orbital reflex motion around the B3 III star. Here we present an analysis of the Hα emission line that is formed in the disk surrounding the Be star. We show that the radial velocities associated with the disk do indeed display a small reflex orbital motion (Section 2) as well as profile shape variations that are related to the orbital phase of the inner binary (Section 3). These results imply that the system is a binary that consists of a rapidly rotating Be star and a low-mass, bright companion that is the core of the former mass donor (Section 4).

2. Hα Wing Bisector Velocities

The hydrogen Balmer emission lines form in a Keplerian rotating disk surrounding the Be star, and the profile generally appears as a double-peaked profile (Sigut et al. 2020). The fastest-moving gas is found closest to the star, so the extreme wings of the emission line provide the best proxy of the motion of the underlying star. The Hα emission line is the strongest emission line in the spectrum of HR 6819, so it is the ideal feature to search for evidence of disk velocity variations associated with the orbital motion if the Be star is part of the 40 day binary.

We downloaded the full set of FEROS spectra from Rivinius et al. (2020) for their Set A group from the ESO 1.5 m telescope[1] (12 spectra) and their Set B group from the ESO/MPG 2.2 m telescope[2] (51 spectra). The spectra were rebinned onto a standard wavelength grid in increments of $\log\lambda$ for a reduced spectral resolving power of $R = 25{,}000$ (to increase the signal-to-noise ratio), and they were rectified to a unit continuum by a linear fit to line-free regions over the wavelength range from 6500 to 6700 Å. This spectral window records the Hα $\lambda6563$ emission line plus the photospheric absorption features of C II $\lambda\lambda6578, 6583$ and He I $\lambda6678$.

The first step was to confirm the orbital elements of Rivinius et al. (2020) by measuring radial velocities for the narrow-lined B3 III star (denoted by star 1). We formed cross-correlation functions (CCFs) of the observed spectra and a model spectrum over the range covering the C II and He I features. The model spectrum was derived from the BLUERED spectral grid (Bertone et al. 2008) for solar abundances, $T_{\rm eff} = 17{,}100$ K,

---

[1] https://www.lsw.uni-heidelberg.de/projects/instrumentation/Feros/ferosDB/search.html
[2] http://archive.eso.org/wdb/wdb/adp/phase3_main/form?collection_name=FEROS

Table 1
Radial Velocity Measurements

Date (HJD−2,400,000)	Orbital Phase	V_r (1) (km s^{-1})	V_r (2) (km s^{-1})	V_r^{sub} (2) (km s^{-1})
46967.186	0.029	2.1	…	…
51373.677	0.280	−41.8	17.1	13.8
51374.675	0.305	−48.9	15.4	12.3
51375.653	0.329	−44.2	15.3	12.4
51376.724	0.355	−28.4	13.3	10.8
51378.682	0.404	−30.6	13.4	11.5
51380.824	0.457	−16.0	11.8	10.8
51383.673	0.528	11.3	9.0	9.4
51384.743	0.554	22.2	7.3	8.3
51385.760	0.579	27.1	6.9	8.2
51390.745	0.703	61.8	3.6	6.7
51393.627	0.774	70.7	2.4	5.8
51394.758	0.802	66.4	1.6	5.1
53138.848	0.044	−10.4	6.1	5.7
53139.683	0.065	−16.2	6.7	5.8
53143.808	0.167	−52.7	11.2	8.3
53144.754	0.190	−56.3	13.6	10.3
53149.763	0.314	−53.4	13.7	10.5
53149.766	0.315	−53.4	13.5	10.4
53154.669	0.436	−21.9	8.9	7.7
53159.805	0.563	18.0	2.8	4.2
53160.687	0.585	27.9	4.3	6.1
53162.863	0.639	40.2	−1.9	1.2
53183.549	0.152	−47.6	12.3	9.5
53185.551	0.202	−53.7	13.5	10.2
53187.667	0.254	−55.0	14.3	10.8
53188.688	0.280	−53.0	11.8	8.6
53190.705	0.330	−51.8	12.8	9.9
53194.692	0.428	−29.4	9.3	7.9
53195.564	0.450	−17.3	7.1	6.2
53196.551	0.474	−5.0	7.7	7.2
53197.670	0.502	7.0	6.9	7.0
53199.571	0.549	26.0	4.7	5.8
53202.646	0.626	48.7	1.7	4.2
53204.513	0.672	64.2	0.7	4.0
53205.697	0.701	65.3	−1.0	2.8
53207.502	0.746	71.5	−2.6	1.4
53226.597	0.219	−55.1	15.8	12.2
53230.491	0.316	−45.5	13.4	10.4
53231.570	0.343	−42.0	13.1	10.2
53232.503	0.366	−42.5	13.0	10.3
53239.495	0.539	17.2	6.2	7.0
53240.603	0.567	27.4	4.8	6.2
53243.516	0.639	53.9	2.4	5.2
53244.552	0.665	63.1	1.0	4.1
53245.511	0.688	63.8	1.2	4.4
53246.620	0.716	61.7	0.8	4.6
53247.553	0.739	64.5	0.3	4.2
53248.523	0.763	66.0	0.9	4.9
53254.540	0.912	47.2	2.0	4.8
53255.516	0.936	32.8	3.5	5.6
53256.556	0.962	26.2	5.7	7.2
53258.493	0.010	13.7	8.0	8.2
53259.532	0.036	0.8	9.6	9.2
53260.537	0.061	−8.3	9.8	8.9
53261.542	0.086	−16.5	12.1	10.5
53262.530	0.110	−22.1	13.7	11.6
53263.537	0.135	−39.8	14.2	11.6
53264.568	0.161	−45.1	15.7	12.6
53265.491	0.184	−45.4	16.1	12.9
53269.509	0.283	−54.3	17.6	13.9
53271.515	0.333	−46.1	16.4	13.2
53272.541	0.358	−39.2	15.0	12.3

Table 1
(Continued)

Date (HJD−2,400,000)	Orbital Phase	V_r (1) (km s^{-1})	V_r (2) (km s^{-1})	V_r^{sub} (2) (km s^{-1})
53273.506	0.382	−30.6	13.2	10.9

$\log g = 3.5$, and no rotational broadening (Rivinius et al. 2020). The radial velocities measured from the CCF peaks are presented in Table 1 that lists the heliocentric Julian date of mid-exposure, the orbital phase, and the radial velocities for star 1 (plus wing bisector velocities for the Be star; see below). We also include a single measurement from the far-ultraviolet spectrum obtained with the International Ultraviolet Explorer (IUE; SWP31220) that we measured using the method described by Wang et al. (2018). The orbital elements were then fit using the nonlinear, least-squares program of Morbey & Brosterhus (1974), and the resulting orbital elements are listed in Table 2. These elements are in good agreement with those presented by Rivinius et al. (2020), and in particular, the IUE measurement from 1987 confirms the orbital period they derived. The orbital radial velocity curve is shown in Figure 1 with phase zero defined by the epoch of periastron given in Table 2.

We measured the Hα emission line wing bisector velocity using the Gaussian sampling method described by Shafter et al. (1986). Each observed profile is cross-correlated with a function consisting of oppositely signed Gaussian functions that are separated from line center by an amount dv, and the zero-crossing position of the resulting CCF yields the bisector velocity. We present in column 4 of Table 1 the wing bisector velocities V_r(2) that represent the radial velocity of the Be star (star 2) that is centered in the disk. These velocities are plotted as open circles in Figure 1, and they display the orbital antiphase motion expected for the companion in the 40 day orbit. A restricted orbital fit of the wing velocities was made by fixing all the elements except for the systemic velocity V_0 and semiamplitude K_2, and the results are listed in column 4 of Table 2. The derived value of K_2 was obtained from velocities measured using Gaussian offsets of $dv = \pm 200$ km s^{-1} (bisector at about 25% of peak strength) and Gaussian FWHM = 100 km s^{-1}, and the uncertainty in K_2 reflects the results made with a range of Gaussian separation dv.

The spectrum of star 1 may include a relatively strong Hα absorption component that is blended with the emission component from the Be star disk. The absorption wings of the star 1 component will appear Doppler shifted with the orbit, causing the emission wings to be slightly depressed when the absorption component moves further into the line wing. This periodic swing in net emission wing strength will influence the resulting measurements of the wing bisector. We modeled this line blending process by shifting the model absorption line to the calculated radial velocity for each spectrum and rescaling the line depth assuming that star 1 contributes 45% of the total monochromatic flux. We again used a model from the BLUERED grid (Bertone et al. 2008) that was broadened for a projected rotational velocity of $V \sin i = 48$ km s^{-1} (Zorec et al. 2016). The shifted and rescaled model was then subtracted from the observed spectrum to create a version corresponding to the Be star and disk alone (see Section 3). The wing bisector velocities were measured in the same way for the
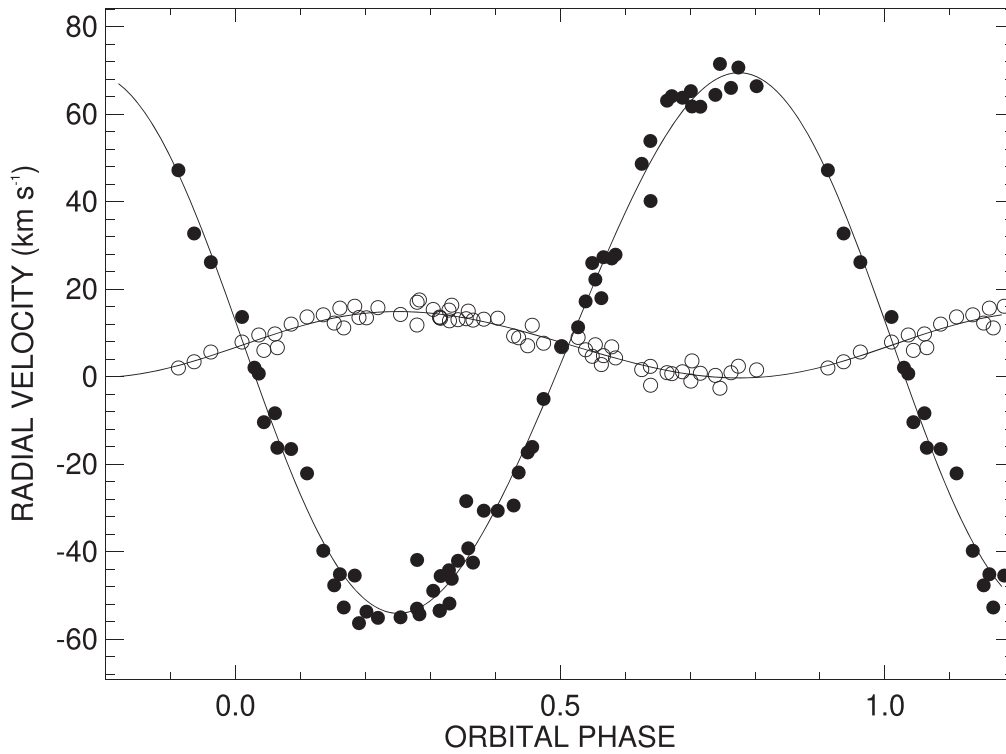
Figure 1. Observed and fitted radial velocity curves for star 1 (filled circles) and star 2 (open circles).

Table 2
Orbital Elements

Element	Rivinius et al. (2020)	$V_r(1)$	$V_r(2)$	$V_r^{\mathrm{sub}}(2)$
P (d) …	40.333 ± 0.004	40.334 ± 0.005	…	…
T (HJD—2,400,000) …	53177.44 ± 0.07	53217.7 ± 2.2	…	…
e …	0.03 ± 0.01	0.039 ± 0.015	…	…
ω (deg) …	89	85 ± 20	…	…
K_1 (km s^{-1}) …	61.3 ± 0.6	61.8 ± 1.0	…	…
K_2 (km s^{-1}) …	…	…	7.6 ± 1.0	3.9 ± 0.7
V_0 (km s^{-1}) …	9.4 ± 0.5	7.5 ± 0.7	7.4 ± 0.9	7.6 ± 0.8
$a_1 \sin i$ ($R_\odot$) …	…	49.2 ± 0.8	…	…
$f(M)$ ($M_\odot$) …	0.96 ± 0.03	0.99 ± 0.05	…	…
r.m.s. (km s^{-1}) …	…	4.8	1.7	2.3

model-subtracted spectra, and these are listed in column 5 of Table 1 under the heading $V_r^{\mathrm{sub}}(2)$. An orbital fit of these velocities for the model-subtracted profiles does indeed yield a smaller but nonzero value of semiamplitude K_2 (column 5 of Table 2). We found that there is an approximate linear relationship between the adopted monochromatic flux scale factor $r = f_1/(f_1 + f_2)$ and the derived semiamplitude, $K_2 \approx (7.5–7.9\ r)$ km s^{-1}. Consequently, in order to reduce the reflex motion to zero, we would need to assume a large flux contribution from star 1, $r = 0.96$. However, this is far outside of the range of possibility based on the appearance of the absorption lines of the Be star that indicate that it (star 2) is a major flux contributor (Rivinius et al. 2020).

The wing bisector radial velocity measurements from both the observed and model-subtracted spectra indicate that the Be disk emission shows the Doppler shifts expected for the companion star in the 40 day orbit. This is compelling evidence that the Be star, and not a black hole, is the orbiting companion of star 1. Rivinius et al. (2020) argued that the Be star lines are stationary, but the small value of K_2 makes it very difficult to

discern the orbital motion of the Be star in the features plotted in Figures 2 and C.2 of their paper.

3. Orbital-phase Variations in Hα Morphology

Be disks are dynamic entities that change on a range of timescales (Rivinius et al. 2013), but we would only expect to observe emission line variations related to orbital phase if the Be star was part of the binary system. The variations of the Hα emission profile as a function of orbital phase are presented in Figures 2 and 3 for the cases of the directly observed profile and the profiles after subtraction of the shifted and scaled model absorption spectrum for star 1, respectively. The top panels show plots of the profiles offset in position according to orbital phase, while the bottom panels show a gray-scale image representation of the profiles as a function of radial velocity and orbital phase (from the time of periastron in the orbital fit given in Table 2). We found that the emission equivalent width was about 38% stronger in the Set A observations from 1999 compared to those in Set B from 2004, so we downscaled the
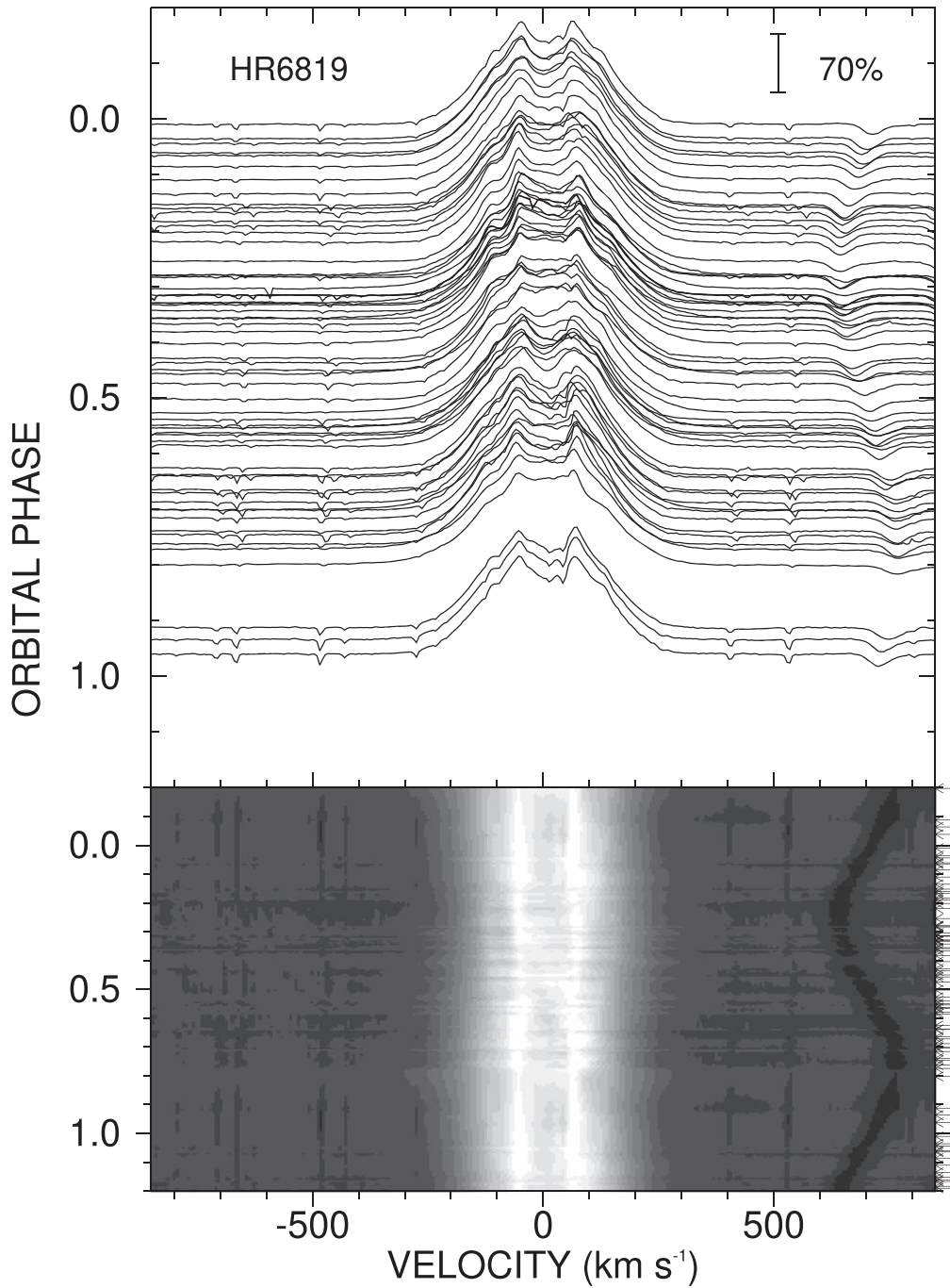
Figure 2. Observed Hα emission line profiles for HR 6819. The top panel shows the individual profiles offset so that the continuum is placed at the orbital phase of observation. The bottom panel shows the same profiles transformed into an image as a function of radial velocity and orbital phase. The absorption component at the right is the C II λ6578 feature in the spectrum of the B3 III star.

emission strength for the 12 spectra from Set A in order to make the comparison with the Set B profiles in Figures 2 and 3.

Both figures show the central violet (V) and red (R) peaks that appear approximately constant in radial velocity. The half-separation between the peaks is 60 km s^{-1}, which matches the semiamplitude of star 1 (K_1 in Table 2). Simple models for Keplerian disks take the half-separation of the peaks as a measure of the projected orbital velocity at the outer boundary of the disk, and the fact that this is the same as K_1 suggests that the outer radius of the disk is comparable in size to the separation between the stars in the binary if star 1 has a small mass (see Section 4). We would generally expect that the disk

outer boundary falls well within the Roche lobe of the Be star, and thus the emission peak half-separation would be larger than K_1 (corresponding to Keplerian motion with smaller radius). However, in cases where the disk has high gas density and the companion has low mass, the disk may extend beyond the companion into a circumbinary configuration (see the case of HR 2142; Peters et al. 2016). Thus, the similarity of the emission peak half-separation and K_1 may indicate that the disk in HR 6819 extends to or beyond the companion.

Figure 3 shows the net emission after subtraction of the blended absorption feature from star 1, and the top panel shows that there are phase-related variations in the V/R peak ratio.
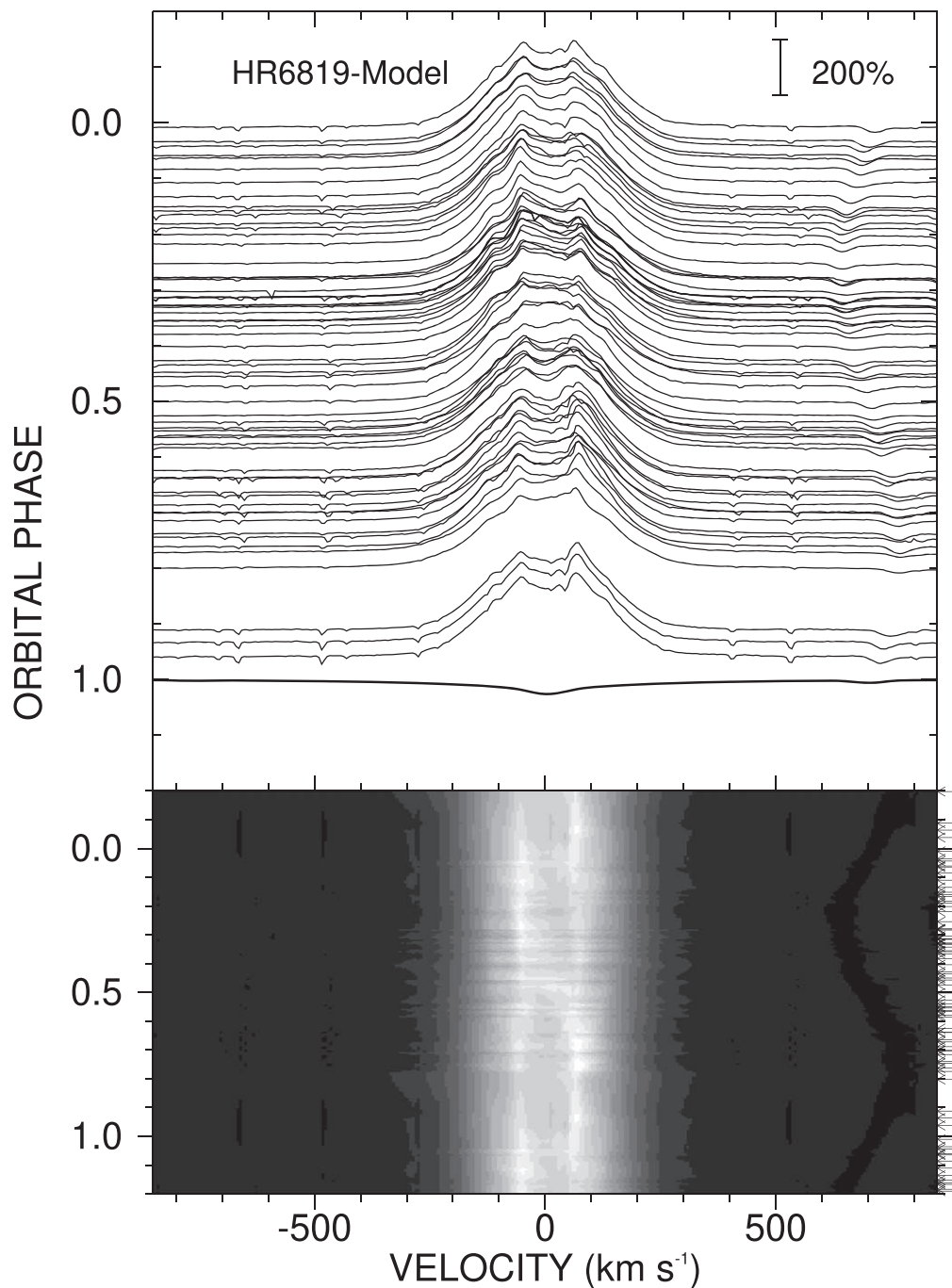
Figure 3. Hα emission profiles after subtraction of a model profile for the absorption component of the B3 III star assuming that it contributes 55% of the monochromatic flux (Rivinius et al. 2020; shown at the bottom of the top panel without Doppler shift).

Near phase 0.25 when star 1 is blueshifted, $V/R > 1$, while the reverse is observed at phase 0.75. This implies that the disk density has an azimuthal asymmetry with greater emission (larger gas density) in the region of the disk facing the companion.

Both Figures 2 and 3 show evidence of small emission enhancements in the lines wings that alternate in the blue and red wings twice per orbit. These generally appear near an absolute radial velocity of $\approx 100\,\mathrm{km\,s^{-1}}$ at the orbital phases of the radial velocity extrema, and the enhancements move to lower velocity as time progresses. These kinds of moving features are also observed in the Be binary HD 55606, and they are interpreted as the result of a two-arm spiral density wave in the disk caused by the tidal force of the companion (Chojnowski et al. 2018). The inner part of the spiral arm appears first at higher velocity, and as the orbit progresses the outer parts of the trailing arms create Doppler shifts at the lower Keplerian velocities found at larger disk radius.

The presence of orbital-phase-related variations in the emission line shape can only be explained if the Be star is part of the binary system and the changes are related to the orbital Doppler shifts and binary-induced disk structure.
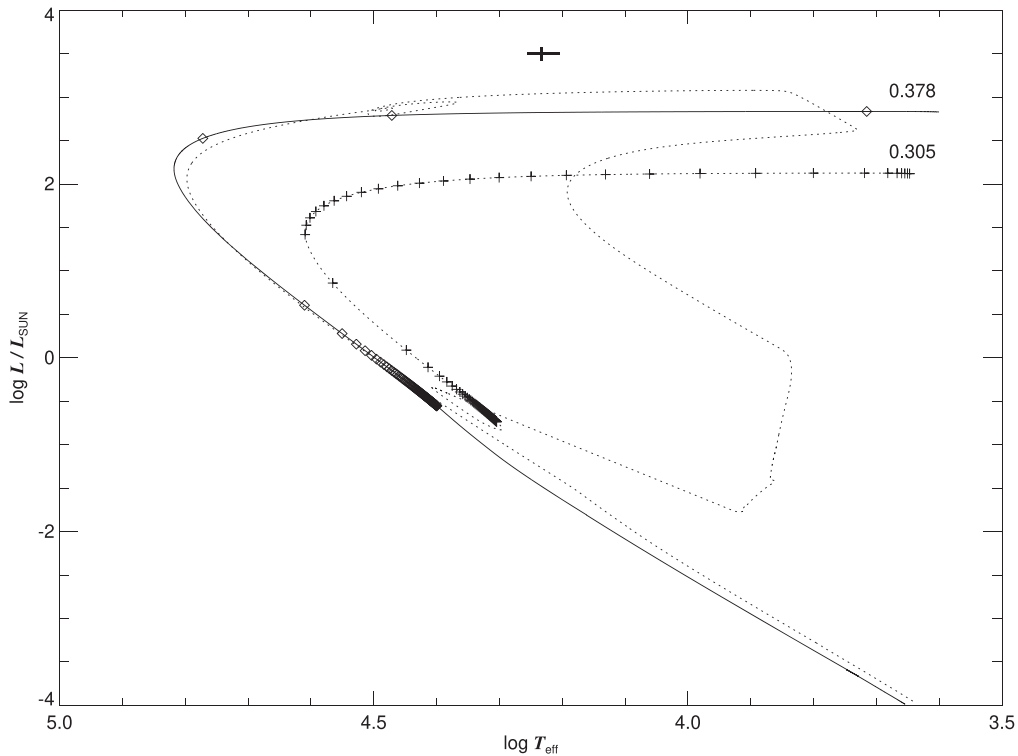
Figure 4. Evolutionary tracks in the ($\log T_{\mathrm{eff}}$, $\log L/L_{\odot}$) plane for models of a $0.305\,M_{\odot}$ (dotted line) and a $0.378\,M_{\odot}$ (solid line) stripped core from the work of Istrate et al. (2016). Diamonds and plus signs mark the locations at increments of 0.1 Myr from the starting point in the model (top right) to an elapsed time of 10 Myr (center). The cross at the top shows the estimated parameters for the B3 III star in HR 6819.

4. Binary Model for HR 6819

Rivinius et al. (2020) examined the system masses by assuming a mass for the B3 III (star 1) component. Given the evidence above that the Be star is the more massive component of the 40 day binary, it is useful to discuss the system properties by considering a probable mass of the Be star. Rivinius et al. (2020) suggest that the Be star is slightly hotter and has a higher gravity than the B3 III star, so we assume that Be star has properties associated with a B2.5 V star: $M_2/M_{\odot} = 6$ and $R_2/R_{\odot} = 3.5$ from the spectral calibration of Pecaut & Mamajek (2013). The mass ratio derived from the radial velocities (Table 2) is $M_1/M_2 = K_2/K_1 = 0.06$ for the model-subtracted case and 0.12 for the directly observed case. Then the implied orbital inclination from the orbital mass function and mass ratio is $i \approx 35°$. This relatively low inclination is consistent with the moderate value of the Be star projected rotational velocity $V \sin i \approx 180\ \mathrm{km\,s}^{-1}$ (from the broad He I line components illustrated in Figure 2 and C.2 in Rivinius et al. 2020), so that the actual equatorial velocity is large, $(V \sin i)/\sin i \approx 310\ \mathrm{km\,s}^{-1}$, similar to that found in many Be stars.

The mass of the B3 III star is in the range $0.4\,M_{\odot}$ (model-subtracted case) to $0.8\,M_{\odot}$ (directly observed), much lower than is typical for stars of this classification. Rivinius et al. (2020) estimate that the star has an effective temperature $T_{\mathrm{eff}} = 17$ kK, luminosity $\log L/L_{\odot} = 3.5$, and radius $R/R_{\odot} = 6$. Based upon the adopted inclination, $i = 35°$, the semimajor axis is $a = 93\,R_{\odot}$, and the stellar radii of both stars are much smaller than their respective Roche radii.

We suggest that the B3 III star has a low mass because it is the stripped down remains of what was originally the mass donor prior to the completion of mass transfer. Istrate et al. (2016)

present models for the evolution of such precursors to He white dwarf stars, and we show in Figure 4 the evolutionary tracks for the two largest core remnant masses in their basic grid for solar metallicity stars. The cores initially grow in temperature at nearly constant luminosity before fading as they approach the white dwarf cooling sequence. In some cases, the models indicate that the cores will experience episodic H-shell burning episodes that will lead to periods of increased luminosity. We also show the location of the B3 III star in HR 6819 at the top of the ($\log T_{\mathrm{eff}}$, $\log L/L_{\odot}$) diagram. By extrapolation to the higher luminosity of the B3 III star, the evolutionary models appear to indicate a mass of $M_1/M_{\odot} = 0.44$ that is consistent with the estimates given above. We note that the implied gravity from the mass and radius is $\log g = 2.5$, which is smaller than that derived by Rivinius et al. (2020) of $\log g = 3.5$ from spectroscopic diagnostics. However, the radius of the B3 III star may need revision once the relative flux contribution of the star is better determined.

The evolutionary tracks in Figure 4 are marked by diamonds ($0.378\,M_{\odot}$) and plus signs ($0.305\,M_{\odot}$) at intervals of 0.1 Myr, and the stripped companion in HR 6819 falls near to the stage in the $0.378\,M_{\odot}$ model where the star crosses the diagram at constant luminosity in only ≈ 0.1 Myr. This indicates that we observe the system at a young, fleeting, and uncommon stage in its post-mass-transfer evolution.

Our examination of the Hα emission line in the spectrum of HR 6819 shows that the Be star disk varies in Doppler shift and line shape with the orbital phase. Consequently, the underlying Be star is the probable companion of the low-mass B3 III in the 40 day orbit. The HR 6819 binary shares many of the characteristics found in other Be + He core systems (in particular, mass ratio and orbital period), but the companions

are usually much fainter and hotter than the Be host stars (Wang et al. 2018). The luminous and low-mass companion in the HR 6819 system may represent a rare and important case in which the companion has recently completed mass transfer and has yet to descend to the white dwarf cooling stage of evolution.

After this work was completed, we became aware of two other papers that come to essentially the same conclusion. Bodensteiner et al. (2020) and El-Badry & Quataert (2020) performed spectral disentangling to reconstruct the spectral lines of both components from the composite spectra. Both studies explored spectral reconstructions over a range in test K_2 values, and they found that the χ^2 residuals between the observed and model binary spectra obtained a minimum for $K_2 = 4.0 \pm 0.8 \, \mathrm{km \, s^{-1}}$ and $K_2 = 4.5 \pm 2 \, \mathrm{km \, s^{-1}}$, respectively. These agree within errors with our result $K_2 = 3.9 \pm 0.7 \, \mathrm{km \, s^{-1}}$ after subtraction of a model Hα absorption profile scaled to a 45% flux contribution from the B3 III star.

ORCID iDs

Douglas R. Gies ⓘ https://orcid.org/0000-0001-8537-3583
Luqian Wang (王璐茜) ⓘ https://orcid.org/0000-0003-4511-6800

References

Bertone, E., Buzzoni, A., Chávez, M., & Rodríguez-Merino, L. H. 2008, A&A, 485, 823
Bodensteiner, J., Shenar, T., Mahy, L., et al. 2020, A&A, in press (arXiv:2006.10770)
Chojnowski, S. D., Labadie-Bartz, J., Rivinius, T., et al. 2018, ApJ, 865, 76
El-Badry, K., & Quataert, E. 2020, MNRAS, in press (arXiv:2006.11974)
Istrate, A. G., Marchant, P., Tauris, T. M., et al. 2016, A&A, 595, A35
Morbey, C. L., & Brosterhus, E. B. 1974, PASP, 86, 455
Pecaut, M. J., & Mamajek, E. E. 2013, ApJS, 208, 9
Peters, G. J., Wang, L., Gies, D. R., & Grundstrom, E. D. 2016, ApJ, 828, 47
Pols, O. R., Cote, J., Waters, L. B. F. M., & Heise, J. 1991, A&A, 241, 419
Rivinius, T., Baade, D., Hadrava, P., Heida, M., & Klement, R. 2020, A&A, 637, L3
Rivinius, T., Carciofi, A. C., & Martayan, C. 2013, A&ARv, 21, 69
Shafter, A. W., Szkody, P., & Thorstensen, J. R. 1986, ApJ, 308, 765
Sigut, T. A. A., Mahjour, A. K., & Tycner, C. 2020, ApJ, 894, 18
Wang, L., Gies, D. R., & Peters, G. J. 2018, ApJ, 853, 156
Zorec, J., Frémat, Y., Domiciano de Souza, A., et al. 2016, A&A, 595, A132